

# A far-field airborne radar NDT technique for detecting debonding in GFRP-retrofitted concrete structures

Tzu-Yang Yu, Oral Büyüköztürk\*

*Department of Civil and Environmental Engineering, Massachusetts Institute of Technology, Cambridge, MA 02139, USA*

Received 13 March 2007; received in revised form 3 July 2007; accepted 10 July 2007

Available online 28 July 2007

## Abstract

A far-field airborne radar (FAR) nondestructive testing (NDT) technique integrating inverse synthetic aperture radar (ISAR) measurements and a backprojection algorithm for the condition assessment of glass fiber reinforced polymer (GFRP)-wrapped concrete structures is proposed. The method is directed toward the detection of near-surface defects and delaminations located in the vicinity of GFRP-concrete interface. Normal and oblique incidence measurement schemes were adopted and studied for their effectiveness in detecting near-surface anomalies. This technique is also applied to the detection of rebars in reinforced concrete cylinders. Laboratory measurements in the frequency range 8–12 GHz were made on artificially damaged GFRP-concrete cylinders for validating the concept of this technique. Spatial resolutions (range and cross-range) are improved by integrating radar measurements at different azimuth angles and in different frequencies, and implementing the developed progressive image focusing scheme. The feasibility of the proposed FAR NDT technique for distant inspection is validated through these studies.

© 2007 Elsevier Ltd. All rights reserved.

*Keywords:* Far-field measurement; Radar NDT; Debonding; Damage detection; GFRP

## 1. Introduction

Strengthening and repair of concrete structures has become an important issue for public safety and for effective infrastructure management. Engineering technologies are developed and introduced for extending the service life of concrete structures by means of restoring their design capacity for continuous use and/or upgrading them for possible future challenges from the environment. The use of fiber reinforced polymer (FRP) composites as an externally bonded element to confine the concrete in order to secure the integrity of concrete structures has been proven, both theoretically and practically, to be an effective and efficient strengthening/repair approach. Integration of the new FRP composite with the existing concrete substrate results in the formation of a new structural system. Differences in the material properties

of the two structural components (FRP and concrete) pose challenging problems of predicting the behavior of the integrated structural system. Extensive research effort has been devoted to this active field as reported in the literature on structural engineering, and composite materials and construction.

Construction defects and structural/environmental damages may occur within the FRP-retrofitted concrete structures, and especially, in the vicinity of FRP-concrete interfaces. Construction defects such as trapped air voids or pockets can occur between FRP sheets/plates and concrete substrate during construction. These air voids serve as a region with shear stress discontinuities. Under mechanical effects stress concentrations would develop around such regions, leading to further development of delamination in the interface region and debonding of FRP from the concrete substrate. Structural damages such as concrete cracking or crumbling inside the FRP wrapping, and/or debonding of the FRP sheet from concrete could occur under various degrees of confinement pressure provided by the FRP wrap. This type of failure has been

\*Corresponding author. Tel.: +1 617 253 7186; fax: +1 617 253 6044.

E-mail address: [obuyuk@mit.edu](mailto:obuyuk@mit.edu) (O. Büyüköztürk).

observed in FRP-wrapped concrete specimens [1], and also FRP-wrapped large-scale reinforced concrete structures [2]. Various approaches on the modeling of debonding have been proposed, such as strength approach, semi-empirical and empirical models, and fracture approach [3–5]. In this paper, both construction defects and structural damages are considered as near-surface material separation or debonding in the interface vicinity of the FRP-concrete system.

Assessing the condition of FRP-wrapped concrete structures nondestructively is crucial to the safety. Wrapped concrete core conditions cannot be fully revealed until physical removal of the wrapping system unless the member has already been subjected to substantive damage. Partial or complete removal of the wrapping may, however, pose a danger of structural collapse. For example, a concrete column could appear safe without showing any sign of damage on the FRP wrap, and yet may contain a substantially damaged concrete core or delamination under the wrap. Such scenario could happen when the structure has undergone a modest seismic event damaging the FRP/concrete system while not causing the ultimate failure of the system. That column may not live up to a second seismic event because of the reduced resistance due to the existing invisible damage in the concrete and in the concrete/FRP interface region. While structural damages can occur at several possible locations in the FRP-concrete system, near-surface regions are mechanically favored as the location where failures initiate. Also, environmental (moisture) effects have been shown to lead to debonding [6]. Debonding of FRP sheets which occurs in the near-surface region is considered as the precursor of structural failures, and, therefore, targeted to be detected. Therefore, effective nondestructive testing (NDT) techniques are needed for detecting the presence of debonding in the near-surface region of FRP-concrete systems.

In this paper, a far-field radar NDT technique (FAR NDT) utilizing the distant radar measurements of FRP-wrapped concrete structures for debonding detection is proposed. While various types of FRP are available and used in practice, including aramid FRP (AFRP), carbon FRP (CFRP) and glass FRP (GFRP), this paper only considers the strengthened/retrofitted concrete columns using GFRP. Scaled GFRP-wrapped concrete cylinder specimens with/without artificial defects are designed and manufactured in the laboratory for the validation of the FAR NDT technique. In this paper, first, existing radar NDT techniques, which have been used in different in civil engineering applications, are briefly reviewed. Emphasis is placed on the radar NDT techniques specifically designed for FRP-concrete systems. System design of the proposed radar NDT technique and laboratory far-field inverse synthetic aperture radar (ISAR) measurements of artificially damaged GFRP-retrofitted concrete specimens are then described. Principles of image reconstruction processing, along with the developed progressive focusing scheme

for image resolution, are explained. Imaging results are provided for demonstrating the validity and performance of the proposed radar NDT technique on debonding. The technique is also applied to the detection of rebars in reinforced concrete cylinders. Finally, research findings are summarized and further research issues are discussed.

## 2. Review of existing radar NDT techniques in civil engineering

Radar NDT is a collective term for NDT techniques using electromagnetic (EM) waves within the radio frequency (RF) spectrum range (3 Hz–300 GHz). Most of the radar NDT techniques used in civil engineering applications operate in the range from very high frequency (VHF) (30–300 MHz) to super high frequency (SHF) (3–30 GHz). Radar NDT relies on the reflected signals from the target for ranging and interpretation. Radar signals can be generated by various devices such as horn antenna and waveguide. Despite the difference in the hardware design of radar systems, the measured quantities are essentially the amplitude and the phase of the received radar signals.

### 2.1. General radar NDT applications in civil engineering

The wave properties of reflected radar signals, such as velocity and amplitude, depend on the dielectric properties and geometrical properties (scattering effects) of the target structures. Thus, characteristics of the target structure can be revealed from the reflected signals. Developments of radar/microwave NDT applications in civil engineering may be reviewed in different categories according to the frequencies utilized. Reported applications include the following: (1) material characterization—[7] (0.1–40 MHz); [8] (3 and 10 GHz); [9] (8–12 GHz), (2) bridge pier scour detection—[10] (300, 500, 900 MHz and 1 GHz); [11] (100–500 MHz), (3) void and crack detection—(3a) stone and brick masonries [12] (500, 900 MHz, and 1 GHz); [13] (500, 900 MHz, 1, and 1.5 GHz); (3b) sluices [14] (500 and 900 MHz); (3c) fatigue cracks in steel [15] (24.125 and 33.6 GHz); (3d) concrete cover [16] (1.5 GHz); (3e) concrete cracking [17] (3.4–5.8 GHz); [18] (2–5.8 and 8–12 GHz); [19] (1.5 GHz); [20] (10 GHz), (4) rebar detection—[18] (2–5.8 and 8–12 GHz); [21] (1 GHz), and (5) structural testing and remote sensing—[22] (10 GHz); [23] (5.75 GHz).

Frequencies used for probing underground and underwater objects are usually less than 1 GHz for the sake of better penetration. For detecting anomalies (air voids, rebar) in concrete higher frequencies (greater than 1 GHz) are usually adopted to achieve better resolution. Frequencies chosen for material characterization are widely distributed due to different experimental configurations.

## 2.2. Radar NDT techniques for damage detection in FRP–concrete systems

Several radar NDT techniques for assessing the condition of FRP–retrofitted/wrapped concrete structures have been reported in the literature. Li and Liu [24] applied a bistatic radar NDT system to detect air voids in the interface region between GFRP–epoxy layer/jacket and concrete surfaces. Radar measurements were conducted at 10 GHz using a pair of dielectric lenses for mechanically focusing signals in an inspection distance of 25 cm. The spatial resolution was 10.16 cm in diameter. Artificial defects of size 0.43 cm<sup>2</sup> were reportedly detected at 10 GHz. The imagery of the structure was the assembly of reflection coefficients at various spatial points.

Feng et al. [25] used a horn antenna and a waveguide reflectometer for detecting air voids in the interface region of GFRP–wrapped concrete specimens. Dielectric lenses were applied in an inspection distance of 6.4 cm in X-band. Artificial defects as small as 0.105 cm in concrete were detected at 12.4 GHz. Reflection coefficients at different spatial points were assembled to form the imagery. Later, Kim et al. [26] proposed the use of planar slot antenna arrays for detecting air voids in concrete panel and block specimens. The slot antenna operated in 5.2 GHz with a resolution of 2.5 cm and a penetration depth of 25 cm. The focusing distance was 3 cm. The imagery was the assembly of the coefficients associated with the Hankel function used to decompose reflection coefficient.

Akuthota et al. [27] utilized an open-ended rectangular waveguide probe and near-field radar measurements for detecting disbands and delaminations between CFRP laminate and the concrete substrate. Artificial defects with sizes in the millimeter range were inserted between the CFRP laminate and the concrete substrate. Inspection distances were 0.15–0.3 cm at 10 GHz and 0.3–0.7 cm at 24 GHz.

Most of the reported radar NDT methods for damage detection in concrete and FRP–concrete structures rely on the near-field measurements in which EM waves are essentially cylindrical or spherical. The near-field approach is inherently sensitive to localized defects and damages of the structure since the probing device is placed in a close distance to the surface of the structure. Strong reflection response can also be expected. Advantages of the near-field approach include: (1) finer spatial resolution; (2) less vulnerability to unwanted edge reflection; (3) small size of probing devices/radiators (e.g., antenna, waveguide); and (4) simple calibration scheme [28]. Disadvantages of the near-field approach include: (1) the constraint of short standoff/inspection distance; (2) complex radiation patterns in the near-field region; and (3) degradation in measurement sensitivity due to the surface roughness of the specimen.

The far-field approach, on the other hand, is not constrained by the requirement of accessibility to the structure, neither easily hampered by the surface condition

of the structure. The proposed FAR NDT technique remedies coarse resolution problem by the integration of inverse synthetic aperture radar (ISAR) measurements and tomographic reconstruction (TR) methods. Technical details of this technique will be provided in the following sections.

## 3. FAR NDT technique and system design

### 3.1. Near-field and far-field regions

The pattern of propagating waves that are generated by a source of finite size changes with respect to their traveling distance. A fixed-size observation plane, regardless of its distance from the source, is implicitly assumed in determining the variation of the wave pattern. In the region close to the source (near-field region), a point source produces spherical waves, a line source produces cylindrical waves, and a plane source produces plane waves (plane sources are rarely used in practice). Wave patterns depend on the observation distance from the source in this region. On the other hand, in the region far enough from the source (far-field region), wave patterns are independent of the observation distance from the source. Consequently, two threshold distances are introduced to define the borders of these two regions; namely, near-field distance and far-field distance. In radar applications these distances depend on the size of the aperture (antenna) and the propagation frequency (wavelength). Observation distances which are shorter than the near-field distance fall in the near-field region, while those longer than the far-field distance fall in the far-field region. The region between the near-field and the far-field regions is the intermediate region. The far-field distance  $d_{ff}$  is generally defined by [29]

$$d_{ff} = \frac{2D^2}{\lambda}, \quad (1)$$

where  $D$  is the largest dimension of antenna apertures, and  $\lambda$  is the minimum wavelength. The far-field condition is met when measurement distance (observation, range) is beyond the far-field distance. Variation of the far-field distance with respect to different aperture sizes in the frequency range 8–12 GHz is shown in Fig. 1. High frequency signals (8–12 GHz) are selected for their inherent ability of capturing centimeter range defects, and the size of probing device (horn antenna) is consequently reduced.

Two aperture sizes ( $D_1 = 0.2$  m,  $D_2 = 0.4$  m) are considered. It is shown that, for an aperture of size 0.4 m, a standoff distance of about 13 m is needed to achieve the far-field condition at 12 GHz. The far-field distance decreases rapidly to 3 m when an aperture of size 0.2 m is used instead. Commercially available horn antennas operating in the frequency range 8–12 GHz have aperture sizes 0.2–0.4 m.

Since, mathematically, true plane waves of any frequency can only occur in the infinite distance from point and line sources, the selection of the observation distance

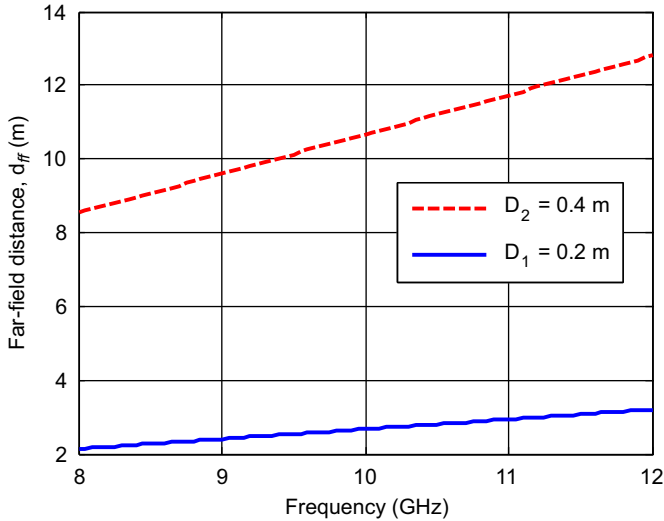


Fig. 1. Far-field distances of two aperture sizes in the frequency range 8–12 GHz.

in the far-field region is associated with certain approximation errors. The wave front error at a given observation distance (or range distance in radar terminology) can be derived:

$$er_{wf}(d) = \left( \frac{Dh}{2} + \frac{D^2}{8} \right) \frac{1}{d}, \quad (2)$$

where  $h$  is the cross-range distance between any two points on the observation plane.  $h$  diminishes when the radar antenna operates in monostatic mode (in this case the transmitter also serves as the receiver). Derivation of Eq. (2) is provided in the Appendix. Eq. (2) leads to the wave front error of  $\lambda/16$  at the far-field distance. A parametric plot is generated, as shown in Fig. 2, for demonstrating the sensitivity of wave front error at different frequencies and observation (range) distances. It is observed that wave front errors become less sensitive to frequency variation when the observation distance is increased to about five times the far-field distance. Resolution in the range direction will be compromised if the far-field condition is not met, and the wave front error becomes significant. It is also noteworthy that, a phase error  $\pi/8$  is associated with the far-field distance since the phase changes  $2\pi$  over a wavelength.

### 3.2. Range and cross-range resolutions

Range resolution is defined on the radial (or range) distance from the radar to the target and is obtained from the transmitted signal. Cross-range resolution is defined as the resolution in the direction perpendicular to the radial direction, and it is obtained by integrating the reflected energy from the target medium as the radar sweeps alongside the area of illumination. Range resolution  $\rho_r$  and cross-range resolution  $\rho_{xr}$  are defined by [30]

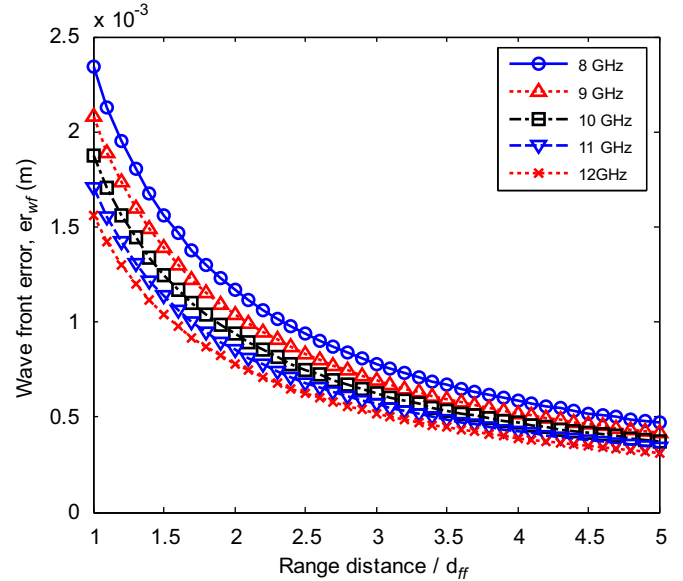


Fig. 2. Wave front errors at different frequencies and at range distances.

$$\rho_r = \frac{v}{2B}, \quad (3)$$

$$\rho_{xr} = \frac{\lambda_c R}{2D}, \quad (4)$$

where  $v$  is the phase velocity of propagating waves in the medium,  $B$  is the bandwidth, and  $\lambda_c$  is the wavelength at center frequency. Eqs. (3) and (4) are the commonly accepted measure of resolution. Better resolutions are achieved when the values of  $\rho_r$  and  $\rho_{xr}$  are reduced. Precise expressions of these resolutions depend on more specific details of the application [31,32]. In a non-magnetic dielectric material (e.g. concrete) these resolutions are given by

$$\rho_r = \frac{(c/\sqrt{\epsilon_r})}{2B}, \quad (5)$$

$$\rho_{xr} = \frac{(c/(f_c\sqrt{\epsilon_r}))R}{2D} \cong \frac{(c/(f_c\sqrt{\epsilon_r}))}{2\theta_{int}}, \quad (6)$$

where  $c$  is the speed of light in free-space,  $\epsilon_r$  is the dielectric constant of the medium ( $\epsilon_r = 1$  in free-space),  $f_c$  is the center frequency, and  $\theta_{int}$  is the angular rotation of the target during processing time. For X-band signals with bandwidth of 4 GHz, the corresponding range resolution in free-space is 3.8 cm. For an aperture of size 0.3 m and angular rotation  $60^\circ$ , the cross-range resolution in free-space is 1.4 cm (X-band). These resolutions become smaller in dielectrics ( $\epsilon_r > 1$ ) because the wavelength becomes shorter as indicated by Eqs. (5) and (6). Thus, damages or defects whose characteristic lengths are comparable to or greater than these values are theoretically detectable. The distance  $d_p$  at which the transmitted EM waves in a medium decays by a factor of  $e^{-1}$  is the penetration depth

(skin depth) and is defined as [33]

$$d_p = \frac{1}{\omega\sqrt{\mu\varepsilon}} \left[ \frac{1}{2} \left( \sqrt{1 + \frac{\sigma^2}{\varepsilon^2\omega^2}} - 1 \right) \right]^{-1/2}, \quad (7)$$

where  $\omega = 2\pi f$  is the radian frequency (rad/s),  $f$  is the temporal frequency (Hz),  $\mu$  is the magnetic permeability (henry/m),  $\varepsilon$  is the electrical permittivity (farad/m), and  $\sigma$  is the electrical conductivity (mho/m). At 8 GHz and 12 GHz,  $d_p$  is estimated to be 4.6 cm and 3 cm, respectively, using the permittivity of  $5.69 \times \varepsilon_0$  ( $\varepsilon_0 \cong 8.85 \times 10^{-12}$  farad/m) (farad/m), and a loss factor  $\sigma/(\varepsilon\omega)$  of 0.62 for concrete.

### 3.3. Inspection schemes

Two ISAR inspection schemes were adopted in this technique: normal incidence (Fig. 3a) and oblique incidence (Fig. 3b). ISAR is an imaging modality using the relative motion of a radar antenna with respect to a stationary target to image that target. This is equivalent to a moving target with a stationary antenna as Figs. 3a and 3b show. Specimens were placed on top of a Styrofoam tower that is capable of fully rotating the target at predetermined angular steps. The radar antenna operated in a monostatic mode. The normal incidence scheme (Fig. 3a) was first applied for damage assessment and rebar detection. In the normal incidence scheme specular return was always encountered regardless of the incident angle ( $\theta$ ). It was found that the specular return in the normal incidence scheme was significant, making it difficult to assess near-surface defects and damages. However, the normal incidence scheme is effective for rebar detection, as

further explained in Section 4.3.  $\zeta$  denotes the position of the antenna on the synthetic aperture.  $\theta_{\text{int}}$  is the range of azimuth angle.

To avoid specular return, oblique incidence scheme is introduced. By tilting the azimuth angle from perpendicular incidence, the intensity of specular reflection response is dramatically reduced when the data are collected in monostatic mode. This way, theoretically, the specular return only dominates the reflection response at  $\phi = 90^\circ$  in the oblique incidence scheme (Fig. 3b). It is worth to point out that other practical factors may widen the angular range, in which significant specular return is still encountered, such as surface smoothness of the structure, shown by the measured frequency–angle data as reported in Section 4.1. In the proposed FAR NDT technique, the oblique incidence scheme is adopted for detecting near-surface defects.

### 3.4. Imaging algorithm and progressive image focusing

The purpose of image reconstruction is to reveal the spatial information from ISAR measurements. The data collection process of ISAR measurements is a linear mapping that transforms the scattering/reflection amplitude data into the range-compressed data. Considering an ideal point scatterer with unit cross section at range  $r$ , the scattering amplitude data  $S(t, r)$  are [34,35]

$$S(t, r) = \frac{B}{r^2} \exp \left[ 2\pi i f_c \left( t - \frac{2r}{c} \right) \right] \times \text{sinc} \left[ B \left( t - \frac{2r}{c} \right) \right], \quad (8)$$

where  $t$  is the elapsed time after pulse transmission,  $B$  is the bandwidth,  $f_c$  is the center frequency,  $c$  is the speed of light (assuming propagating in free space), and  $\text{sinc}(x) = \sin(\pi x)/(\pi x)$ . The range compressed data  $D(\zeta, t)$  of this scattering amplitude data are defined by

$$D(\zeta, t) = \int \int G(x, y) S \left( t, \sqrt{(x - \zeta)^2 + y^2} \right) dx dy, \quad (9)$$

where  $\zeta$  is the radar position along the aperture (Fig. 3a,b),  $G(x, y)$  is the complex scattering amplitude of the target, and  $(x, y)$  forms the image plane. The image reconstruction is another mapping operation that transforms the range-compressed data into the image. The processed image is a filtered version of the spatial profile of the target.

The applied backprojection algorithm is one of the TR methods. The defined backprojection image  $I(x, y)$  is given by

$$I(x, y) = \int_{x-y \tan(\theta_{\text{int}}/2)}^{x+y \tan(\theta_{\text{int}}/2)} F_{\text{BP}} \times \left( \zeta, \frac{2\sqrt{(x - \zeta)^2 + y^2}}{c} \right) d\zeta, \quad (10)$$

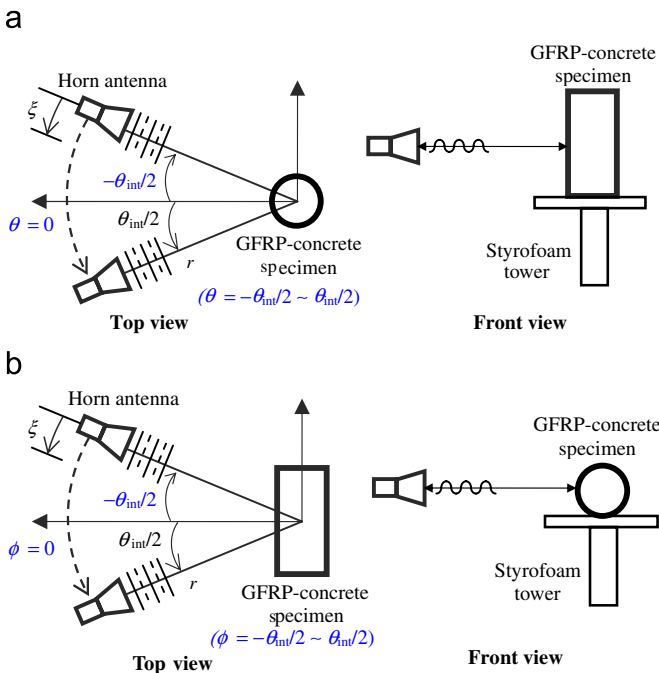


Fig. 3. (a) Normal incidence scheme; (b) Oblique incidence scheme.

where  $F_{BP}(\xi, t) = (8\pi^2/ic^2)(\partial D(\xi, t)/\partial t)$ , and  $\theta_{int}$  is the integral angle of the aperture. Details of backprojection algorithm can be found in the literature of SAR imaging [34–37]. The backprojection image  $I(x, y)$  characterizes the feature of the target in terms of scattering intensity in the range ( $x$ ) and cross-range ( $y$ ) directions. Numerical implementation of the backprojection algorithm is performed based on the fast backprojection algorithm by Yegulap [38]. In this fast backprojection algorithm the data are first divided into several subapertures and processed to generate relatively low-resolution images. The final imagery is formed by summing up all the subaperture images. Consequently, resolution is progressively (gradually) improved. Such processing scheme can be advantageous for NDT of civil infrastructures, especially when different purposes (e.g. preliminary and detailed inspections) of inspection are needed. The magnitude of an image pixel,  $I(\bar{p})$ , at position  $\bar{p}$  is calculated by the backprojection equation:

$$I(\bar{p}) = \sum_{n=1}^{N_s} I_n(\bar{p}) = \sum_{n=1}^{N_s} \int_{-l/2}^{l/2} F\left(s_n + \xi, \frac{2}{c}|\bar{p} - \bar{q}(s_n + \xi)|\right) d\xi, \quad (11)$$

where  $N_s$  is the number of subapertures,  $l$  is the length of subapertures,  $F$  is the measurement data received at position  $(s_n + \xi)$  and time  $(2/c|\bar{p} - \bar{q}(s_n + \xi)|)$ ,  $\xi$  is the distance variable on each subaperture,  $s_n$  is the center point of  $n$ th subaperture, and  $\bar{q}$  is the position vector of aperture points. This image focusing scheme for computationally improving the image resolution is herein termed as *progressive image focusing*.

The concept of *progressive image focusing* is developed for processing the measured data in this study. As opposed to the mechanical focusing technique generally used in near-field NDT applications, with this technique the measured responses are focused by means of data processing along a measurement orbit (aperture) that is suitable for the particular structural configuration. Images can be produced by measured data from subbands and subapertures for a preliminary assessment. Scattering signals due to the presence of defects in reflection response are reconstructed in the images. By superimposing all subband and subaperture images, the resolution is progressively improved as the scattering signals converge. This will be further discussed and demonstrated with an example in Section 4.2.

## 4. Application

The feasibility and performance of this FAR NDT technique is validated and examined in this section using laboratory measurements on GFRP-retrofitted concrete specimens with artificial defects and rebars. The specimens and experimental configuration, together with measure-

ment schemes, are described. Collected frequency–angle data and processed range–cross-range imagery are also provided in this section.

### 4.1. Laboratory ISAR measurements

#### 4.1.1. GFRP-retrofitted concrete specimens

To demonstrate the feasibility of the developed technique, four concrete and GFRP–concrete cylinder specimens were designed and manufactured for laboratory measurements: AD1: GFRP–concrete with artificial defect Type 1, AD2: GFRP–concrete with artificial defect Type 2, RE: concrete with four rebars, and PC: plain concrete. Portland Type I cement was used, and the mix ratio of concrete was water:cement:sand:aggregate = 0.45:1:2.52:3.21 (by weight). The diameter of concrete core was 15.24 cm, and the heights were 30.4 cm and 38.1 cm as shown in Figs. 4a and 4b. Concrete cores of these specimens were cast with different configurations (e.g., artificial defect, rebar) and cured in clean water for 14 days. Artificial defect type 1 was a cubic-like Styrofoam ( $3.81 \times 3.81 \times 2.54 \text{ cm}^3$ ), and artificial defect type 2 was a delamination-like Styrofoam ( $7.62 \times 7.62 \times 0.51 \text{ cm}^3$ ). These two artificial defects were placed in the interface between GFRP sheet and concrete substrate in the GFRP–concrete specimen. After the curing period the concrete cores were wrapped with one layer of GFRP sheet according to the manufacturer's specifications.

A unidirectional glass fabric system (Tyfo<sup>®</sup> SEH-51A by Fyfe Co. LLC) was used and molded with epoxy resin (Tyfo<sup>®</sup> S Epoxy) to form the GFRP–epoxy sheet wrapped on the surface of the concrete core. The volumetric ratio of epoxy:GFRP was 0.645:0.355. The thickness of the GFRP–epoxy sheet was 0.25 cm. Single layer configuration scheme was adopted. GFRP–concrete specimens AD1 and AD2 are shown in Fig. 4a.

Specimen RE was manufactured with four #3 steel rebars (diameter = 0.95 cm) positioned at four angles with different cover depths ( $0^\circ$ : 0.25/ $90^\circ$ : 1.27/ $180^\circ$ : 2.54/ $270^\circ$ : 3.81 cm). Fig. 4b shows specimens RE and PC.

#### 4.1.2. Laboratory configuration and measurement schemes

Radar measurements of the GFRP–confined concrete specimens were performed at MIT Lincoln Laboratory using the Compact RCS/Antenna Range facility. The experimental set-up consists of a horn antenna, stepped-frequency radar, network analyzer systems, and a Harris dual-shaped reflection system, Model 1606, designed for conducting far-field measurements. The purpose of this reflection system is to produce plane waves in the limited space of laboratory. A schematic description of laboratory configuration is provided in Fig. 5. The reflection system would not be required for field measurements. This facility can achieve high signal-to-noise ratio (SNR) for a large frequency bandwidth ranging from UHF (0.7 GHz) to 100 GHz. The radar system is capable of producing a 20-m quiet zone, different antenna radiation patterns, and full

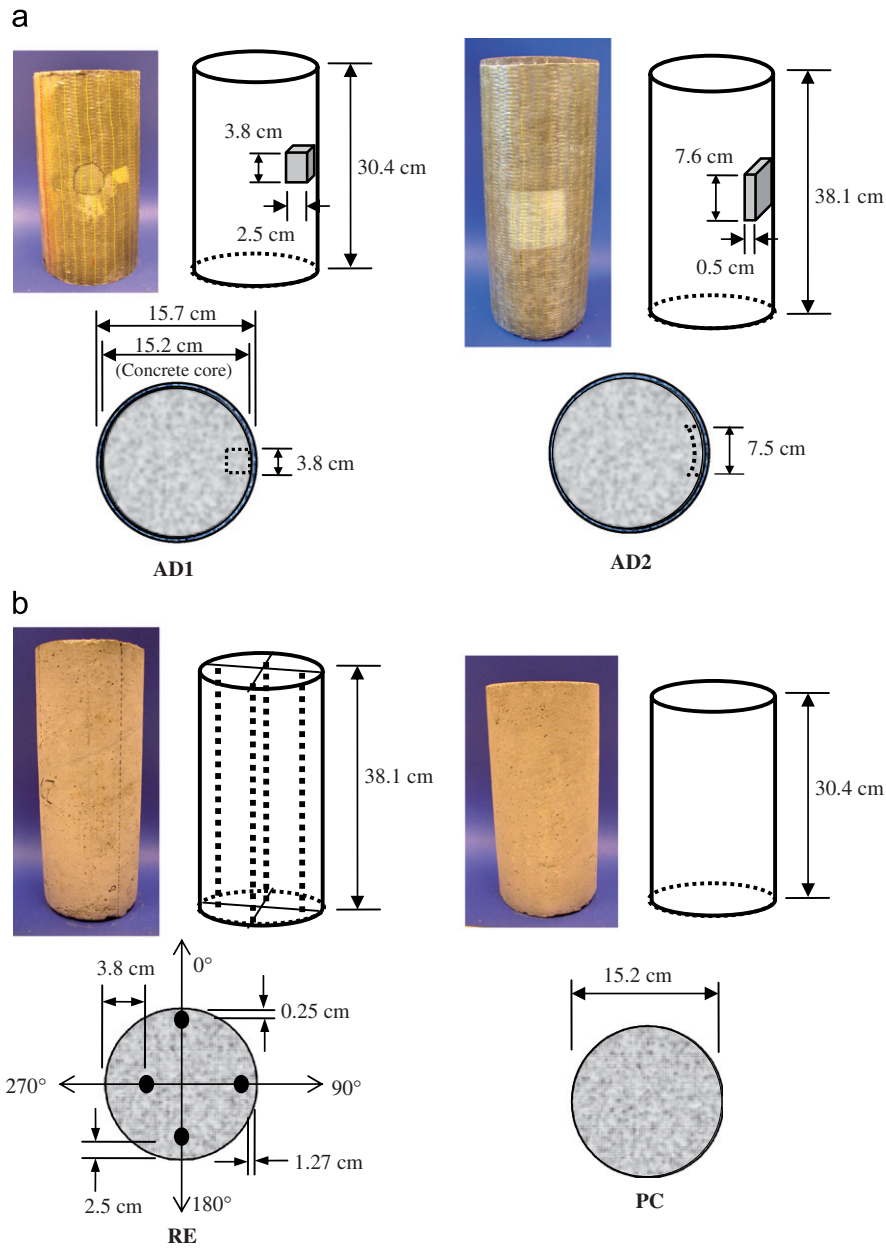


Fig. 4. (a) GFRP-concrete specimens AD1 and AD2; (b) Concrete specimens RE and PC.

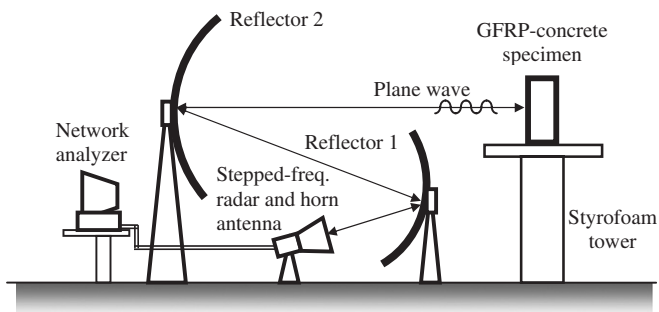


Fig. 5. Schematic description of the laboratory experimental configuration.

polarimetric radar cross section (RCS) measurements. Calibration of the far-field measurement is carried out with respect to the surface of the target structure. SNR is enhanced by the coherent, wide bandwidth measurements in this technique.

Radar measurements were conducted at X-band (8–12 GHz) frequencies to achieve optimized resolution and surface penetration capabilities. Two types of linear polarizations were used in the radar measurements: HH (transverse electric or TE) and VV (transverse magnetic or TM). Sinusoidal signals were used, and steady-state responses were collected.

4.1.3. Frequency–angle data

The measurements were conducted in stepped-frequency mode by sweeping from a starting frequency to an end frequency in an increment of 0.02 GHz at a fixed angle. The specimen was then rotated to the next angular step, and the frequency sweeping was again performed (Fig. 3a,b). The total rotation (range of azimuth angle),  $\theta_{int}$ , in the ISAR measurements was  $30^\circ$  and  $60^\circ$ , and the angular increment was  $0.2^\circ$ . Frequency–angle data showing the reflection response in decibel (dB) were obtained and recorded.

Normal incidence scheme was used on the specimens RE and PC; the frequency–angle data measured at X-band in HH polarization are shown in Fig. 6. Significant differences are observed in normal incidence reflection responses between plain concrete specimen and the specimen with rebars.

Oblique incidence scheme was used on specimens AD1 and AD2 for near-surface damage detection. Both the intact surface (without artificial defect) and the damaged surface of the specimen AD1 were measured, while only the damaged surface of the specimen AD2 was measured. Collected frequency–angle data of the intact and damaged

surfaces of the specimen AD1 are shown in Fig. 7. It is seen that, specular return dominates the reflection response at azimuth angles around  $\phi = 0^\circ$  (from  $-2^\circ$  to  $2^\circ$ ).

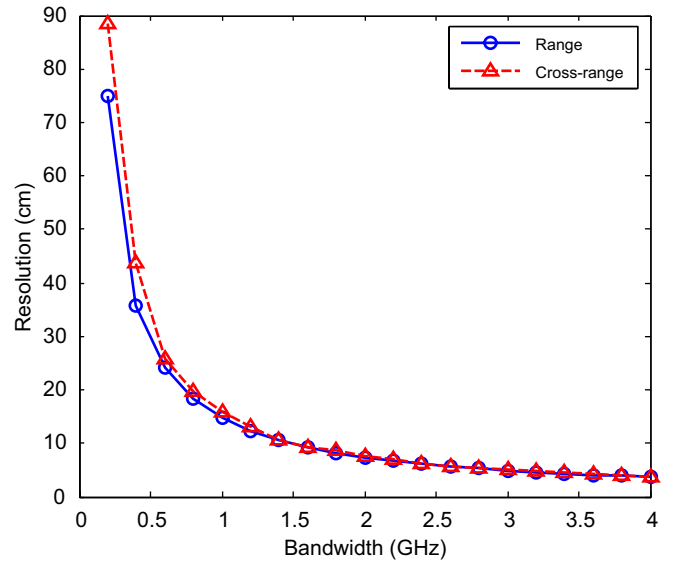


Fig. 8. Range and cross-range resolutions versus bandwidth.

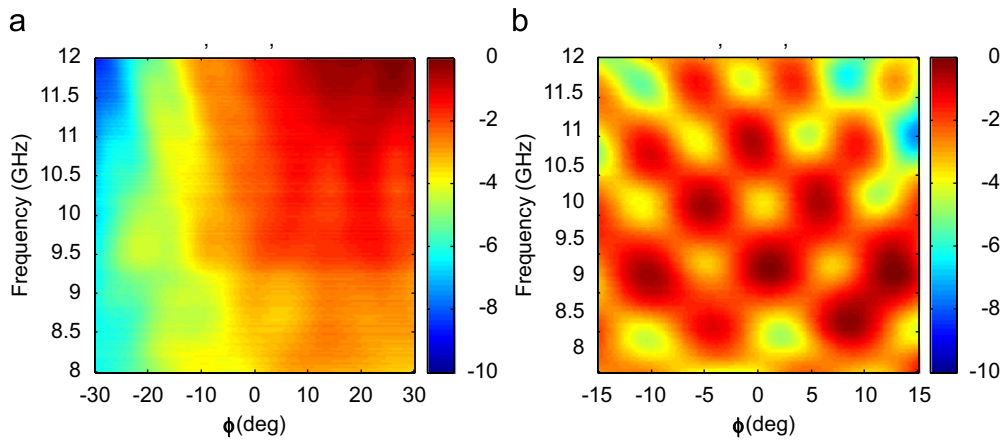


Fig. 6. Frequency–angle data of specimens PC and RE, HH polarization, X-band, normal incidence scheme: (a) specimen PC; (b) specimen RE.

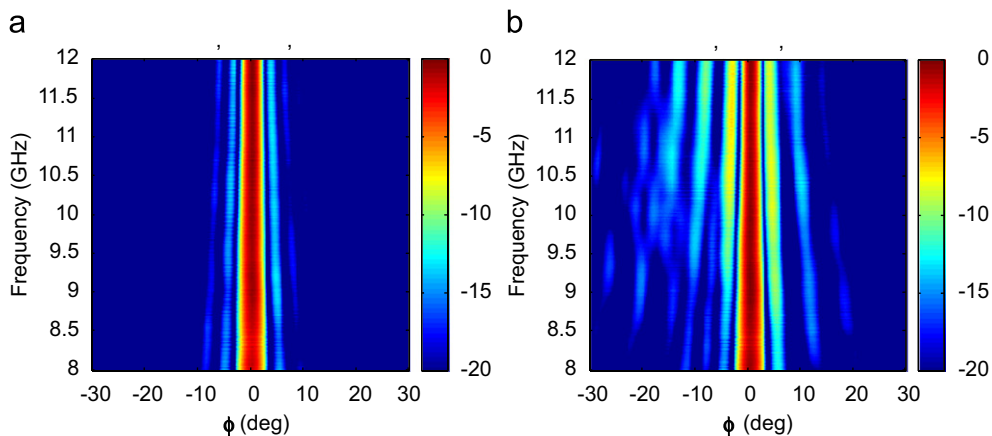


Fig. 7. Frequency–angle data of the intact and damaged surfaces of the specimen AD1, HH polarization, X-band, oblique incidence scheme: (a) intact surface; (b) damaged surface.

The specular return is reduced to a significant degree when azimuth angle deviates from  $\phi = 0^\circ$ . The spreading signals in Fig. 7b indicate the presence of a near-surface artificial defect in the specimen AD1. Fig. 7 demonstrates the effectiveness of the use of the oblique incidence scheme in eliminating the specular return. The radar measurements on the specimen AD2 also showed scattering signals similar to those obtained for the specimen AD1.

4.2. Progressive image focusing

Image reconstruction is performed through the progressive image focusing in conjunction with the use of the oblique incidence ISAR data for the intact surface of the specimen AD1. In this application, Eqs. (5) and (6) suggest

that near-surface debonding damages with characteristic lengths 3.72 cm (range) and 3.76 cm (cross-range) are theoretically detectable beyond a far-field distance 10 m with bandwidth 4 GHz (center frequency 10 GHz) using a horn antenna with aperture size 0.4 m (Fig. 8). This improvement of resolution is quantitatively evaluated with respect to frequency bandwidth in Fig. 8. It is shown that, in Fig. 8, the range and cross-range resolutions of the far-field ISAR measurements are dramatically improved with increasing bandwidth.

The measurements are processed to render the images in Fig. 9. Bandwidth of each image is increased from the upper left image (0.44 GHz) to the lower right image (4 GHz), with frequency band indicated in each image. In Fig. 9, the features of the specimen are gradually revealed

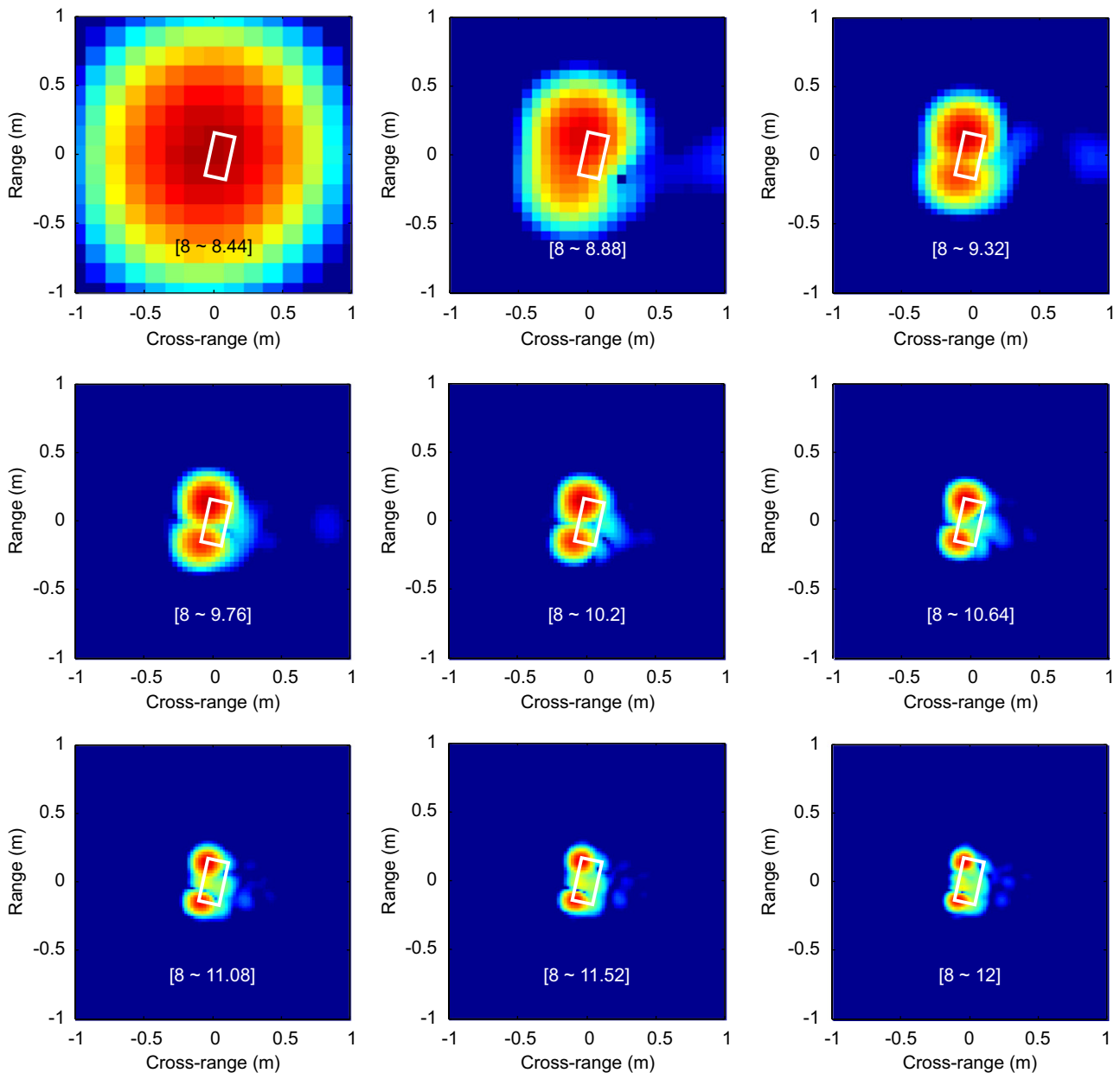


Fig. 9. Processed images of the intact surface of the specimen AD1 with different bandwidths.

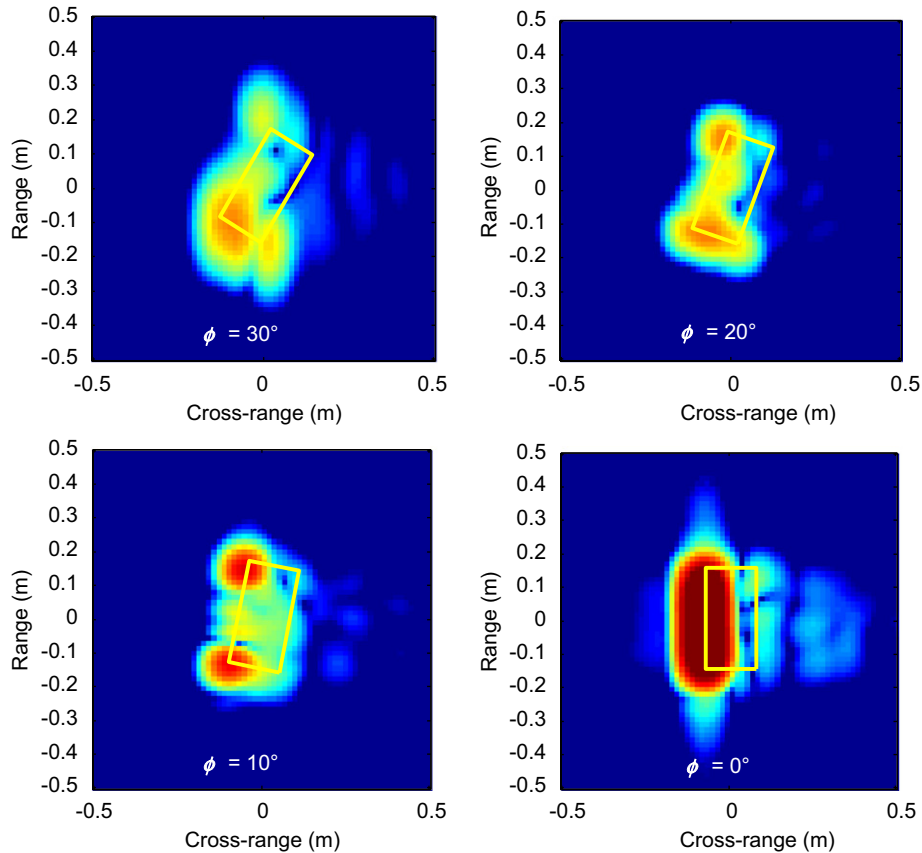


Fig. 10. Backprojection images of the GFRP–concrete specimen AD1—intact surface ( $\phi = 30^\circ\text{--}0^\circ$ ).

by the converging of scattering signals in the images. Two scattering signals representing the effect of the two ends of the specimen are identified in the upper middle image with bandwidth 0.88 GHz. This feature becomes clearer in other images with wider bandwidths. Although 4 GHz bandwidth is presumably suggested, geometric features of the specimen are visually detectable when the bandwidth is only about 1 GHz (Fig. 9). This implies that, by taking the advantages of ISAR measurement and back-projection algorithm, the ability of the imagery to capture the features of the target structure can be increased if *a priori* knowledge on the shape and size of the target structure is available. This is the case for preliminary inspection where the global features would be first revealed at narrow bandwidths. Therefore, the detection ability of the imagery is believed to be higher than theoretical values as shown in Fig. 9. This feature also makes the proposed radar NDT technique promising for in-field applications.

### 4.3. Condition assessments

#### 4.3.1. Debonding detection

For detecting debonding defects the two artificially damaged GFRP–concrete specimens (AD1, AD2) are subjected to radar measurements in the oblique incidence scheme. Both HH and VV polarizations of radar signals

are used but only HH polarization results are reported here. The far-field ISAR measurements on the intact (without defect) and damaged (with defect) surfaces of the specimen AD1 are collected, while only the damaged surface of the specimen AD2 is measured. For the intact surface and damaged surface responses of the specimen AD1 the processed backprojection images at various incident angles are shown in Figs. 10 and 11. The specimen boundaries are indicated in solid yellow lines in Figs. 10–12. In this case, unlike the normal incidence scheme in which specular returns are always significant at all incident angles  $\theta$ , specular returns are only significant when  $\phi$  equals  $90^\circ$  due to the monostatic operation of the radar antenna. The alleviation of specular returns in the oblique incidence scheme provides an opportunity to discover unseen, hidden near-surface defects such as FRP debonding, or concrete delamination in the interface region.

The imagery produced from the reflected responses of the GFRP–concrete specimens with anomalies contain two types of recognizable scattering signals: (1) edge reflections of the specimen (Figs. 10–12) and (2) reflections from the defect and debonding in the near-surface region of the specimen (Figs. 11 and 12). The reconstructed image only reveals the edge reflections of the specimen when there is no defect in the specimen, as shown in Fig. 10. The two edge reflections of the specimen in the imagery (e.g., image

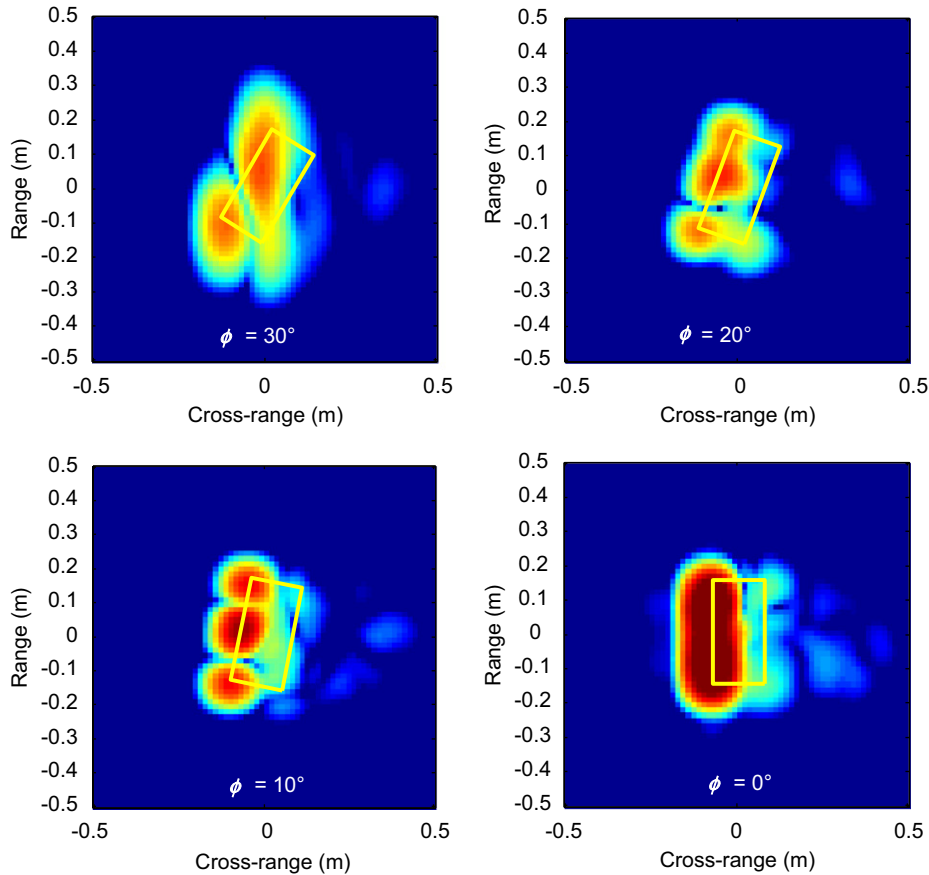


Fig. 11. Backprojection images of the GFRP–concrete specimen AD1—damaged surface ( $\phi = 30^\circ\text{--}0^\circ$ ).

$\phi = 10^\circ$  in Fig. 10) represent the two ends of the specimen AD1, and can be used for determining the size of the cylinder specimen. Also, these end reflections can be used as reference points to determine defect locations in the specimen. Note that the influence of unwanted edge reflections in the imagery would diminish with the increased specimen or structure dimensions.

Fig. 11 shows both the edge and the existing defect reflections from the specimen AD1 when measured from the damaged surface. The cubic defect is revealed in the image (e.g., image  $\phi = 10^\circ$  in Fig. 11) as a strong scattering signal whose peak indicates the center of the cubic defect (Type 1). Using the full bandwidth (4 GHz), the imagery of the specimen AD2 with delamination reveals the detailed features of the anomaly as shown in the  $\phi = 10^\circ$  image in Fig. 12. By providing sufficient bandwidth and angular coverage in the inspection, detailed features of defects with smaller sizes may also be detectable.

The effectiveness of the chosen azimuth angle on the detectability of the imagery is also demonstrated in Figs. 10–12. In each figure it is observed that there is a range of azimuth angles in which the defect can be more effectively detected than in other angular ranges. For example,  $\phi = 10^\circ$  gives the best result for damage detection in Fig. 11. This suggests that the detectability of the technique is sensitive to the chosen inspection angle.

#### 4.3.2. Rebar detection

The capability of detecting steel rebars by the proposed FAR NDT technique is demonstrated in this section. The normal incidence ISAR measurements of the cylinder specimens RE (plain concrete with four rebars) and PC (plain concrete) are collected in the X-band (8–12 GHz). These far-field measurements are then processed to render imagery for rebar detection. The backprojection images of the specimen PC are shown in Fig. 13 with white solid lines indicating the location of the specimen.

For the specimen RE far-field responses are made at four incident angles corresponding to the location of each rebar:  $0^\circ$ ,  $90^\circ$ ,  $180^\circ$ , and  $270^\circ$  (Fig. 4b). Rebars, horn antenna, and the center of the specimen form a straight line at these angles. Since specular return is much stronger than the reflected signal of the rebar at these angles, the scattering signal of the rebar is “shadowed” by the specular return and, therefore, the rebars are not directly detectable. However, it is found that the scattering signals of adjacent rebars are not masked by the specular return, as shown in the case of incident angle equals  $0^\circ$  (Fig. 14). This observation is clear in both HH and VV polarizations. By using the backprojection algorithm on processing the normal incidence ISAR data, two scattering signals adjacent to the specular return signal are revealed at the locations where two adjacent rebars are physically

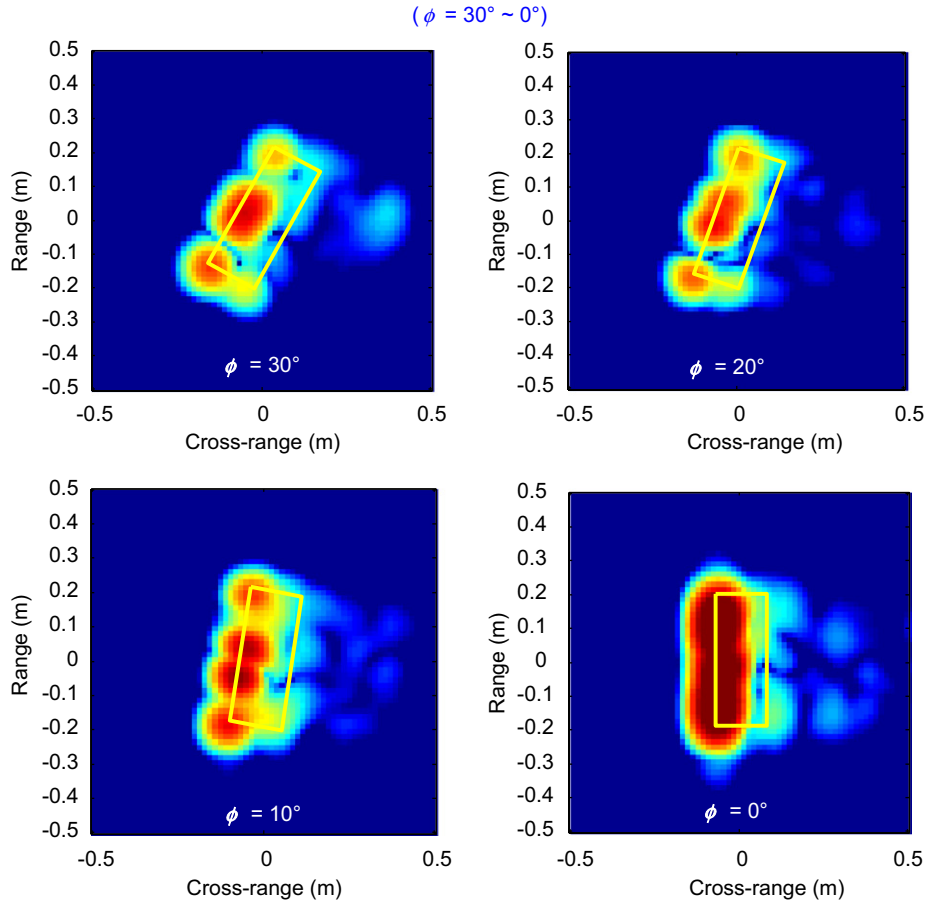


Fig. 12. Backprojection images of the GFRP–concrete specimen AD2—damaged surface ( $\phi = 30^\circ\text{--}0^\circ$ ).

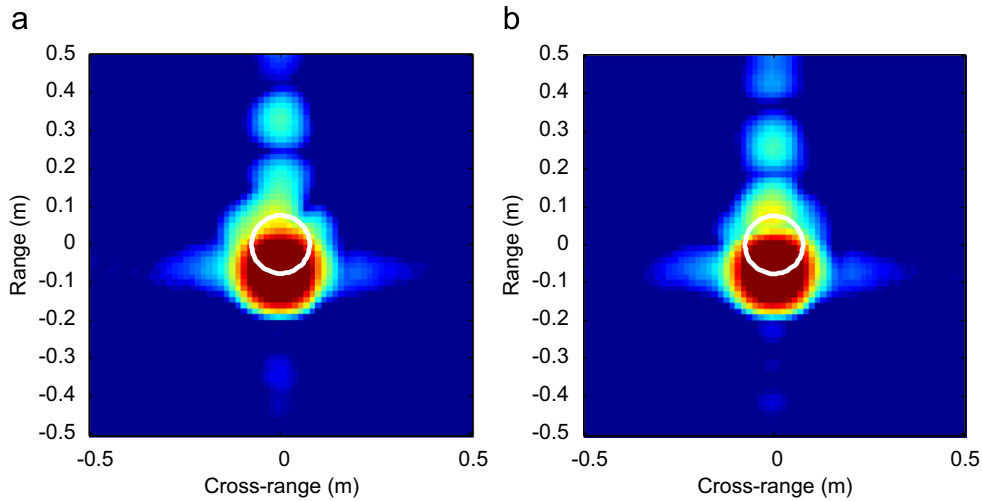


Fig. 13. Backprojection images of the specimen PC: (a) HH polarization; (b) VV polarization.

embedded. In other words, normal incidence scheme can be used to detect the location of rebars, except the one right in front of the radar. It is expected that the shadowed rebar can be revealed when the inspection region of radar moves to another one. Imagery of incident angles  $90^\circ$ ,  $180^\circ$ , and  $270^\circ$  also provide similar results, and thus, are not

repeatedly reported here. It is noteworthy to point out that, the size (or the coverage) of specular return depends on the used frequency bandwidth in this technique, as previously suggested in Fig. 9. Using the normal incidence scheme for detecting rebar locations must be associated with sufficient frequency bandwidth. In addition, HH

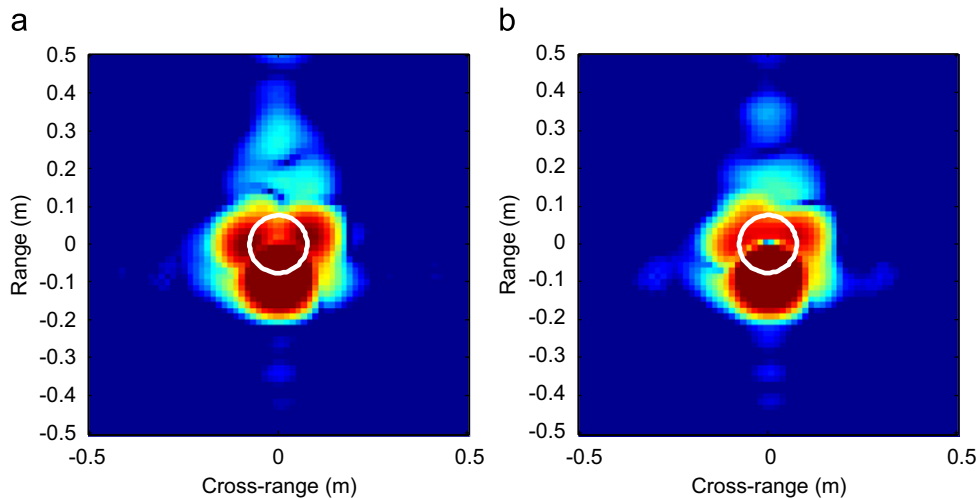


Fig. 14. Backprojection images of the specimen RE at  $0^\circ$ : (a) HH polarization; (b) VV polarization.

polarization is found to be more effective for illuminating the presence of adjacent rebars than VV polarization since the HH imagery show stronger scattering signals of the rebars than the VV imagery. The comparison between Figs. 13 and 14 validates the rebar detection capability provided by this FAR NDT technique.

## 5. Conclusion

The proposed FAR NDT technique for NDT of GFRP-wrapped concrete structures consists of two components: (1) far-field ISAR measurements in two schemes, and (2) image reconstruction algorithm. In this paper, work is reported on laboratory radar measurements of GFRP–concrete specimens in the far-field region at different angles in the frequency range 8–12 GHz. The measured frequency–angle data are processed by the imaging algorithm (backprojection algorithm) to reconstruct the range–cross-range imagery of the structure, which serves as a basis for condition assessments to detect near-surface defects and debonding, as well as rebars in the specimen. Research findings are summarized as follows:

- (1) *Validity of the technique*—This work validates the feasibility of the proposed FAR NDT technique for distant inspection of GFRP–concrete structures. It is shown that, with optimized bandwidth and angular ranges, near-surface defects including air voids and delaminations as well as existing rebars may be well-detected.
- (2) *Computational focusing*—Spatial resolutions (range and cross-range) are improved by integrating radar measurements at different azimuth angles and in different frequencies, and implementing the developed *progressive image focusing* scheme. With this scheme, the reconstructed imagery efficiently captures the features of the target structure, especially when *a priori* knowledge (shape and size) of the structure is available.

This is the case when preliminary inspection is first performed since with such an inspection global features of the structure would be revealed at narrow bandwidths. Detailed inspection can then be conducted, given additional data at different azimuth angles and in different frequencies. Thus, this feature potentially enables the proposed FAR NDT technique for effective in-field applications.

- (3) *Rebar detection using the normal incidence scheme*—The specular return dominates the reflection response in the normal incidence scheme for both HH and VV polarizations. Near-surface defects are unlikely to be revealed in such incidence scheme. However, although the presence of the rebar placed in front of the radar is masked by the strong specular returns from the surface, the presence of adjacent rebars can be clearly captured in the imagery, regardless of polarization. In addition, HH polarization is found to be more effective than VV polarization in terms of the amplitude of scattering signals in the imagery.
- (4) *Debonding detection using the oblique incidence scheme*—Specular returns are only significant in the perpendicular incidence case ( $\phi = 0^\circ$  in Figs. 10–12) due to the monostatic operation of the radar. The alleviation of specular returns in the oblique incidence scheme provides an opportunity to discover unseen near-surface defects in GFRP–retrofitted concrete systems. Thus, the reconstructed imagery clearly separates damage signals from edge reflection signals.
- (5) Only GFRP–retrofitted concrete specimens are studied in this paper. Nonetheless, the methodology is considered applicable to other concrete systems with different types of fiber such as carbon (graphite) and aramid. Strong shielding effect of unidirectional carbon fibers in the reflected radar signals can be alleviated by the use of EM waves orthogonally polarized to the direction of fiber orientation.

## Acknowledgments

This work was supported by the National Science Foundation through Grant CMS-0324607, and by the MIT Lincoln Laboratory through Grant ACC-376 (Advanced Concepts Committee). Wide-bandwidth radar measurements were performed at the MIT Lincoln Laboratory under the supervision of Dennis Blejer. We gratefully acknowledge his efforts and contributions to the research reported in this paper. We also express our appreciation to Prof. J.A. Kong, Prof. D.H. Staelin and Dr. T.M. Grzegorzczak at MIT, and Prof. M.C. Forde at the University of Edinburgh (UK) for many valuable discussions. Finally, the authors thank Fyfe Co. LLC for supplying the materials used in the experimental work.

## Appendix A

Consider a simple radar antenna aperture model in Fig. A.1 where S stands for the source point, O is the observation point, A is the edge point, and B is the center point of the antenna with respective radial distances of  $r$  and  $r + \delta r$ . Points A and B are chosen for the maximum difference in the radiation patterns at these two points. In the far-field region, the difference between these distances should be insignificant such that (i) the radiation pattern of the antenna is angular independent, and (ii) the wavefront difference diminishes. Condition (i) suggests a circular radiation pattern, and condition (ii) suggests the plane wave pattern at an observation point. In monostatic radar measurements, observations are always made at one point, making the measurements less affected by the overall radiation pattern of the antenna. Therefore, condition (ii) is adopted for evaluating the error (wave-front difference) associated with the selected distance in the far-field region.

The wave-front difference at points A and B with respect to the observation point O is calculated by

$$\Delta = (r + \delta r) - r = \sqrt{d^2 + (h + a)^2} - \sqrt{d^2 + h^2}, \quad (\text{A.1})$$

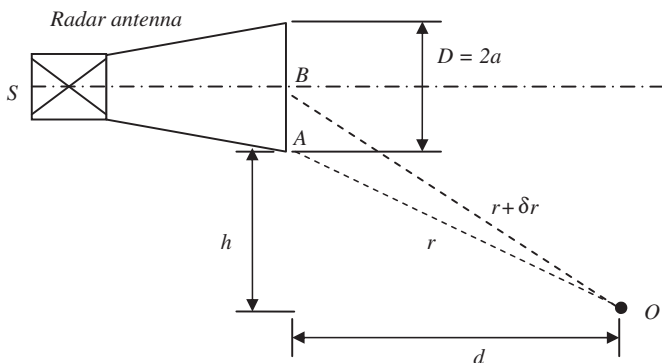


Fig. A.1. A simple aperture model.

The first-order Taylor's series expansion of Eq. (A.1) provides

$$\begin{aligned} \Delta &\cong d + \frac{(h + a)^2}{2d} - d - \frac{h^2}{2d} \\ &= \frac{(h + a)^2}{2d} - \frac{h^2}{2d} = \frac{h}{d}a + \frac{1}{2d}a^2. \end{aligned} \quad (\text{A.2})$$

Should the waves be perfectly planar, there is no wave-front difference at the observation point O between the waves sent from points A and B. According to this, the plane wave condition is interpreted by

$$\Delta = 0, \quad (\text{A.3})$$

which is theoretically correct at infinite distance ( $d \rightarrow \infty$ ). At the distances other than infinity, this difference is not exactly zero. In the far-field region, the wave-front difference descends with increasing distance  $d$ . Thus, it is used for evaluating the plane wave condition at a distance  $d$  in the far-field region. The wave-front error  $er_{wf}$  associated with the distance is then

$$er_{wf} = \left( ah + \frac{a^2}{2} \right) \frac{1}{d} = \left( \frac{Dh}{2} + \frac{D^2}{8} \right) \frac{1}{d}, \quad (\text{A.4})$$

since  $a = D/2$  as shown in Fig. A.1.

## References

- [1] Au C, Büyüköztürk O. Effect of fiber orientation and ply mix on fiber reinforced polymer-confined concrete. *J Compos Constr* 2005;9(5): 397–407.
- [2] Sheikh SA, Yau G. Seismic behaviour of concrete columns confined with steel and fibre reinforced polymers. *ACI Struct J* 2002;99(1): 72–80.
- [3] Buyukozturk O, Gunes O, Karaca E. Progress on understanding debonding problems in reinforced concrete and steel members strengthened using FRP composites. *Constr Build Mater* 2004;18: 9–19.
- [4] Teng, JG. Debonding failures of RC beams flexurally strengthened with externally bonded FRP reinforcement. In: Proceedings of Eleventh International Conference and exhibition of structural faults + repair 2006, Scotland, UK: University of Edinburgh; 2006.
- [5] Büyüköztürk O, Yu T.-Y. Understanding and assessment of debonding failures in FRP-concrete systems. In: Proceedings of seventh international congress on advances in civil engineering. Istanbul, Turkey: Yildiz Technical University; 2006.
- [6] Au C, Büyüköztürk O. Peel and shear fracture characterization of debonding in FRP plated concrete affected by moisture. *J Compos Constr* 2006;10(1):35–47.
- [7] Al-Qadi IL, Hazim OA, Riad SM. Dielectric properties of Portland cement concrete at low radio frequencies. *J Mater Civil Eng* 1995; 7(3):192–8.
- [8] Bois KJ, Benally AD, Zoughi R. Microwave near-field reflection properties analysis of concrete for material content determination. *IEEE Trans Instrum Meas* 2000;49(1):49–55.
- [9] Arunachlam K, Melapudi VR, Upda L, Upda SS. Microwave NDT of cement-based materials using far-field reflection coefficients. *NDT E Int* 2006;39(7):585–93.
- [10] Millard SG, Bungey JH, Thomas C, Soutos MN, Shaw MR, Patterson A. Assessing bridge pier scour by radar. *NDT E Int* 1998; 31(4):251–8.
- [11] Forde MC, McCann DM, Clark MR, Broughton KJ, Fenning PJ, Brown A. Radar measurement of bridge scour. *NDT E Intl* 1999; 32(8):481–92.

- [12] Binda L, Lenzi G, Saisi A. NDE of masonry structures: use of radar tests for the characterization of stone masonries. *NDT E Int* 1998; 31(6):411–9.
- [13] Maierhofer Ch, Leipold S. Radar investigation of masonry structures. *NDT E Int* 2001;34(2):139–47.
- [14] Maierhofer Ch, Krause M, Wiggenhauser H. Non-destructive investigation of slucies using radar and ultrasonic impulse echo. *NDT E Int* 1998;31(6):421–7.
- [15] Qaddoumi N, Ranu E, McColskey JD, Mirshahi R, Zoughi R. Microwave detection of stress-induced fatigue cracks in steel and potential for crack opening determination. *Res Nondestr Eval* 2000;12:87–103.
- [16] Klysz G, Balayssac J-P, Laurens S. Spectral analysis of radar surface waves for non-destructive evaluation of cover concrete. *NDT E Int* 2004;37(3):221–7.
- [17] Büyüköztürk O, Rhim HC. Radar measurements of concrete for nondestructive evaluation of dams. In: *Proceedings of SPIE, 1995*; 2457: 168–74.
- [18] Rhim HC, Büyüköztürk O. Wideband microwave imaging of concrete for nondestructive testing. *J Struct Eng* 2000;126(12):1451–7.
- [19] Maierhofer Ch, Brink A, Rollig M, Wiggenhauser H. Detection of shallow voids in concrete structures with impulse thermography and radar. *NDT E Int* 2003;36(4):257–63.
- [20] Nadakuduti J, Chen G, Zoughi R. Semiempirical electromagnetic modeling of crack detection and sizing in cement-based materials using near-field microwave methods. *IEEE Trans Instrum Meas* 2006;55(2):588–97.
- [21] Shaw MR, Millard SG, Molyneaux TCK, Taylor MJ, Bungey JH. Location of steel reinforcement in concrete using ground penetrating radar and neural networks. *NDT E Int* 2005;38(3):203–12.
- [22] Shinozuka M, Ghanem R, Houshmand B, Mansouri B. Damage detection in urban areas by SAR imagery. *J Eng Mech* 2000;126(7): 769–77.
- [23] Pieraccini M, Luzi G, Mecatti D, Fratini M, Noferini L, Carssimi L, et al. Remote sensing of building structural displacements using a microwave interferometer with image capability. *NDT E Int* 2004;37(9):545–50.
- [24] Li J, Liu C. Noncontact detection of air voids under glass epoxy jackets using a microwave system. *Subsurf Sens Tech Appl* 2001;2(4): 411–23.
- [25] Feng MQ, De Flaviis F, Kim YJ. Use of microwave for damage detection of fiber reinforced polymer-wrapped concrete structures. *J Eng Mech* 2002;128(2):172–83.
- [26] Kim YJ, Jofre L, De Flaviis F, Feng MQ. Microwave reflection tomographic array for damage detection of civil structures. *IEEE Trans Antennas Prop* 2003;51(11):3022–32.
- [27] Akuthota B, Hughes D, Zoughi R, Myers J, Nanni A. Near-field microwave detection of disband in carbon fiber reinforced polymer composites used for strengthening cement-based structures and disbond repair verification. *J Mater Civil Eng* 2004;16(6): 540–6.
- [28] Zoughi R, Lai J, Munoz K. A brief review of microwave testing of stratified composite structures: a comparison between plane wave and near-field approaches. *Mater Eval* 2001;60(2):171–7.
- [29] Botsco RJ, Cribbs RW, King RJ, McMaster RC. Microwave methods and applications in nondestructive testing. In: *nondestructive testing handbook—electromagnetic testing: eddy current, flux leakage, and microwave nondestructive testing*. Columbus, OH: American Society of Nondestructive Testing, vol. 4; 1986. Section 18.
- [30] Knott EF, Shaeffer JF, Tuley MT. *Radar cross section*. Raleigh, NC: SciTech Publishing Inc; 2004.
- [31] Blitz J. *Electrical and magnetic methods of non-destructive testing*. New York, NY: Chapman & Hall; 1997.
- [32] Balanis CA. *Antenna theory: analysis and design*. New York, NY: Wiley; 1997.
- [33] Kong JA. *Electromagnetic wave theory*. Cambridge, MA: EMW Publishing; 2000.
- [34] Carrara WG, Goodman RS, Majewski RM. *Spotlight synthetic aperture radar—signal processing algorithms*. Boston, MA: Artech House; 1995.
- [35] Soumekh M. *Synthetic aperture radar signal processing with MATLAB algorithms*. New York, NY: Wiley; 1999.
- [36] Skolnik MI. *Radar handbook*. New York, NY: McGraw-Hill; 1990.
- [37] Desai MD, Jenkins WK. Convolution backprojection image reconstruction for spotlight mode synthetic aperture radar. *IEEE Trans Image Proc* 1992;1(4):505–17.
- [38] Yegulalp AF. Fast backprojection algorithm for synthetic aperture radar. In: *Proceedings of IEEE radar conference, 20–22 April 1999*. p. 60–5.